IEEE Access
Multidisciplinary | Rapid Review | Open Access Journal

Received July 9, 2020, accepted July 16, 2020, date of publication July 27, 2020, date of current version August 6, 2020.

Digital Object Identifier 10.1109/ACCESS.2020.3011915

A New Workflow for Image-Guided Intraoperative Electron Radiotherapy Using Projection-Based Pose Tracking

SUBHRA S. GOSWAMI[1,2], JUAN E. ORTUÑO[1,2], ANDRÉS SANTOS[1,2], (Senior Member, IEEE), FELIPE A. CALVO[3], JAVIER PASCAU[4,5], (Member, IEEE), AND MARÍA J. LEDESMA-CARBAYO[1,2], (Member, IEEE)

[1]Biomedical Image Technologies Laboratory, ETSI Telecomunicación, Universidad Politécnica de Madrid, 28040 Madrid, Spain
[2]Biomedical Research Networking Center in Bioengineering, Biomaterials and Nanomedicine (CIBER-BBN), Carlos III Health Institute, 28029 Madrid, Spain
[3]Department of Radiation Oncology, Clinica Universidad de Navarra, 28027 Madrid, Spain
[4]Departamento de Bioingeniería e Ingeniería Aeroespacial, Universidad Carlos III de Madrid, 28911 Madrid, Spain
[5]Instituto de Investigación Sanitaria Gregorio Marañón, 28007 Madrid, Spain

Corresponding author: Subhra S. Goswami (subhra@die.upm.es)

This work was supported in part by the Spanish Ministry of Science and Innovation under Project TEC2015-66978-R (MINECO/FEDER, EU) and Project RTI2018-098682-B-I00 (MCIU/AEI/FEDER, EU); in part by the European Commission under European Regional Development Fund and European Social Fund; and in part by the Ministerio de Ciencia e Innovación, Instituto de Salud Carlos III, Spain, under Grant PI18/01625 and Grant PI15/02121.

ABSTRACT A new workflow is proposed to update the intraoperative electron radiotherapy (IOERT) planning refreshing the position and orientation (pose) of a virtual applicator with respect to the preoperative computed tomography (CT) with the actual pose during surgery. The workflow proposed relies on a robust registration of the preoperative CT and intraoperative projection radiographs acquired with a C-arm system. The workflow initially performs a geometric calibration of the C-arm using fiducials placed on the applicator. In the next step, a point-based 2D–3D registration based on fiducials positioned on the patient's skin is performed, followed by an intensity-based registration that refines the point-based registration result. The performance of the workflow has been evaluated using a realistic physical phantom consisting of a pig lower limb and its corresponding CT and 7 C-arm projections at different poses. The accuracy has been measured with respect to the applicator origin and axis before and after the registration refinement process. A feasibility study with human data is also included. Error analysis revealed angular accuracy of 0.9 ± 0.7 degrees and translational accuracy of 1.9 ± 1 mm. Our experiments demonstrated that the proposed workflow can achieve subdegree angular accuracy in locating the applicator with respect to the preoperative CT to update and supervise the IOERT planning right before radiation delivery. The proposed workflow could be easily implementable in a routine, corresponding to a significant improvement in quality assurance during IOERT procedures.

INDEX TERMS 3D-2D registration, IGIOERT, image guided intra operative electron radiotherapy, IOERT, IORT.

I. INTRODUCTION

Radiotherapy has a long history since X-rays were discovered in 1895 [1]. With gradual progress, in the standard practices of radiotherapy procedures, cancer patients would need to undergo radiation therapy for five days a week for up to three to six weeks after surgery. With the advancement of radiation devices, delivering radiation at the time of surgery was attempted for the first time after 1960 [2]. Since then, the surgeons started delivering radiation directly to the tumor bed where the tumor has just been removed while the area is exposed during surgery to destroy any lingering microscopic cancer cells during the procedure. This procedure is called intraoperative radiotherapy (IORT). IORT is usually delivered in combination with external-beam radiation therapy with/without chemotherapy. IORT is typically performed

The associate editor coordinating the review of this manuscript and approving it for publication was Larbi Boubchir.

without image-based treatment planning. The current standard of care shows that delivering high doses of radiation precisely to the tumor bed with minimal exposure to the surrounding healthy tissues is possible with IORT based on the experience of the radiation oncologist, being guided by the surgery itself and his or her vision and touch [3], [4]. The collaboration with biomedical engineering could benefit the technique by providing innovative solutions based on image-based approaches for preplanning, intraplanning, and documenting of the procedure [3], [5].

Several methods can be used to deliver IORT. IORT can be delivered using electron beams (IOERT), orthovoltage (250–300 kV) X-rays (X-ray IORT), high-dose-rate brachytherapy (HDR-IORT), or low-energy (50 kV) X-rays (low-energy IORT). Because of a more uniform dose distribution of the electron beam, limited depth of penetration directly to the target volume, and short treatment time, IOERT has become more popular than the other techniques [6]. IOERT applies a single-fraction high dose of electron beam radiation directly to the target volume through an applicator that is fixed between the linear accelerator (LINAC) and the target location of the patient. The applicator size provides safe coverage of the target volume at the delivered dose by considering the cross-sectional profiles at the selected electron energy.

The applicators used for IOERT have a cylindrical shape with a diameter varying between 3 cm and 12 cm. These are made of sterilizable polymethyl methacrylate with a thickness of 5 mm or anodized aluminum cylindrical tubes. The length of the applicator varies from 32 cm to 100 cm [7]. The applicator may have a bevel for cases in which the tumor bed presents at some angle to the horizontal that is not within the LINAC's range of motion. The bevel helps the applicator adjust better to the resected area and be placed in the accurate position and orientation (pose) for yielding the best dose delivery [8], [9]. The base angle of this bevel changes between 0° and 45°. Alternative applicator designs have been proposed in [10], [11]. They follow the recommendations and design of commercial applicators but include modifications to improve the positioning in a soft-docking accelerator [10] or to increase the dose homogeneity by using a scattering foil [11].

Treatment parameters such as applicator dimension, bevel angle, pose, or beam energy are planned before the surgery by interacting with a virtual environment using preoperative images while considering the surgical scenario and clinical experience of the radiation oncologists [12]. The radiation oncologists need to modify the original plan during surgery to minimize the risk of irradiating critical structures and to ensure the target radiation in the proper location. The retraction of structures and removal of the cancerous tissues of the targeted organ produces geometrical and anatomical modifications. Several software tools exist [13]–[15] that can be used for IOERT planning before surgery where the applicator can be virtually positioned on a CT image to maximize the dose delivered to the target volume and minimize its effect on the organs at risk, typically using Monte Carlo dose estimations.

The general method to ensure correct patient placement and treatment verification for many image-guided surgery procedures is to register preoperative images to intraoperative images using fiducial markers on the patient skin or the different structures in the surgery room. Typically, 3D CT data are considered as preoperative images. Intraoperative 3D CT or 3D fluoroscopy could mean an advantage in complex surgical procedures as these methods can provide improved accuracy and reliability [16] because of the 3D nature of the data and their better contrast between structures. However, 3D CT or fluoroscopy systems are rarely available in surgery rooms and imply longer procedures and higher radiation exposure. Meanwhile the 2D projection C-arm system [17] is typically available and used as intraoperative data. Current research on image-guided surgery uses intraoperative 2D projections for planning, guidance and verification because they provide an accurate depiction of the internal structures, anatomical deformation, and resection within the region of interest, as well as the required instrumentation during the procedure [18]–[20](Markelj, Tomazvic *et al.* 2012). However, to represent the 3D coordinate reference system properly, multiple views are needed [21]. For this purpose, specifically, designed fiducial markers are used for estimating the C-arm pose from intraoperative 2D C-arm radiograph images [22], [23].

As an alternative, researchers have shown that the C-arm pose and the positions of surgical tools can be estimated using external tracking systems such as optical measurement devices these methods have been recently applied to locate the applicator in IOERT [24], [25]. However, this approach has several limitations related to the size of the optical tracking systems and the potential line-of-sight occlusions between the tracking device and the optical tracker during the procedure. Moreover, some external tracking systems take a long time to calibrate. Electromagnetic tracking [26], [27] could also be used during IOERT because it does not have the disadvantage of the line-of-sight, but on the other hand, the presence of any electronic devices may produce significant interferences and disturb the process [28]. In both cases, the tradeoff between system accuracy and working volume may be another consideration that may present limitations.

Given its potential advantages regarding usability and providing information about the internal structures, we believe that the intraoperative 2D image guidance of the IOERT procedure could enable proper therapy surveillance of radiotherapy delivery during surgery. Our work focuses on providing proper localization of the applicator with respect to the target while tackling the following specific issues: 1) problems arising from the use of external trackers, 2) inaccuracies in reaching the target, 3) registering the applicator position at radiation delivery and updating the planning enabling dose accumulation computation at organs at risk. To our knowledge, there is no previous workflow that has solved all these issues together.

The alignment process of the 2D intraoperative and the 3D preoperative image should be approached following a 2D–3D registration framework. 2D–3D medical image registration methods have been used for the last decades in other image-guided scenarios and can be divided into three types: feature-based [29], gradient-based [30]–[32] and intensity-based [33], [34]. Feature-based methods depend on the segmentation of anatomical structures, and this segmentation is a challenging task to perform fully automatically. Gradient-based methods are usually driven by attenuation coefficient gradients found in the edge of bony structures in preoperative CT that point to intensity gradients of intraoperative X-ray images. They rely on the fact that the strong intensity gradients in X-ray images correspond to boundaries of bony structures in the CT, but they also have a very narrow convergence. Intensity-based registration requires less complex preprocessing but requires a good initialization to avoid local minima. Three 2D–3D approaches are followed based on the image dimensions and spatial correspondences: (a) projecting 3D images into 2D space for 2D–2D registration, (b) back-projection of 2D points to 3D space, and (c) reconstruction of 3D images from 2D projections for 3D–3D registration [35]. Most image-guided procedures lean toward intensity-based 2D to 3D projective registration because it requires less projection and is less computationally expensive.

For 2D–3D intensity-based registration, a similarity measure must be defined. Comparative studies [36], [37] show that metrics based on local intensity correspondence tend to outperform those based on global intensity. Otake *et al.* [38] initially proposed the use of the gradient correlation (GC) similarity metric because it is independent of the image dynamic range, and they later concluded that gradient difference (GD) and pattern intensity (PI) are the most accurate and robust metrics against outliers [21]. According to Wu *et al.* [30], normalized cross-correlation (NCC) and normalized mutual information are robust methods for megavoltage imaging, whereas PI, GD, and GC are the most accurate. These authors also reported that NCC is both accurate and robust for kV X-ray imaging. Gendrin *et al.* [39] and Otake *et al*. [40] concluded that in the presence of soft tissues and deformations, gradient-based metrics are more accurate and robust.

II. CONTRIBUTIONS OF THIS PAPER

In this work, we propose a complete protocol and image processing workflow to update the IOERT spatial planning during surgery to ensure an accurate estimation of dose distribution and treatment verification without using an external tracking system. To achieve this goal, we calculate the relative pose between the intraoperative C-arm radiographs and the preoperative CT image used for the IOERT planning to finally position a virtual applicator in the preoperative CT, mimicking the actual position during surgery.

We use a set of radiopaque fiducials attached to the patient's skin around the area of interest and onto the IOERT applicator, and these fiducials are automatically detected in the C-arm intraoperative radiographs to provide an initial pose estimation. Later, a robust refinement process based on 2D–3D intensity-based registration between the C-arm radiographs and the preoperative CT image's digitally reconstructed radiographs (DRRs) provides a more accurate solution that uses the point-based registration using fiducial markers as a robust initialization.

To assess the feasibility, we performed experiments using a realistic physical phantom made using a pig lower limb. We investigated the accuracy of 3D localization and the required angular separation between projection image pairs to be used in the workflow. An experiment conducted using patient data has also been performed as a proof of concept of the proposed workflow in the clinical scenario.

III. METHODS

A. PROBLEM DEFINITION AND PROPOSED WORKFLOW

The proposed protocol updates the IOERT planning during surgery performed using exclusively a preoperative CT scan and the 2D radiographs obtained with a C-arm system in the intraoperative scenario. With the premise that a suitable system should minimize the use of additional calibration procedures or external tracking devices, the proposed protocol uses only an applicator with fiducials and fiducials on the patient's skin both during preoperative and intraoperative acquisitions.

The image-guided IOERT navigation protocol has the following steps: (a) radiopaque landmarks are placed on the patient's skin and on the applicator; (b) a preoperative CT of the patient's ROI is acquired; (c) the OR intraoperative fluoroscopic projections are acquired; (d) the segmentation of fiducials in all 3D and 2D images is performed; (e) the surgery is performed, removing the cancerous tumor; (f) the LINAC and the attached applicator are placed in an initial position; (g) the image processing workflow follows to find the transformation between IOERT applicator and patient. This helps to track the applicator in the real scenario and display over the preoperative CT scan; (h) the updated position and orientation of the applicator are assessed with respect to the prescribed treatment plan and the dose distribution is calculated; (i) LINAC delivers the prescribed dose to the target volume through the applicator. The image processing workflow for the presented IGIOERT protocol is defined using the following steps: (a) the pose estimation of the C-arm intraoperative radiographs, relative to the IOERT applicator, taken as a common reference; (b) initial pose estimation of a virtual applicator in the preoperative scenario using point-based registration; (c) refinement of this initial result using a 2D–3D intensity-based registration of the intraoperative C-arm radiographs and the preoperative CT image.

This workflow guides the oncologists to accurately position the virtual applicator in the preoperative CT according to the actual situation during the intraoperative scenario, allowing the updating of the radiation planning and the verification

of the IOERT treatment without using an external tracking system. The proposed protocol is described in Fig. 1.

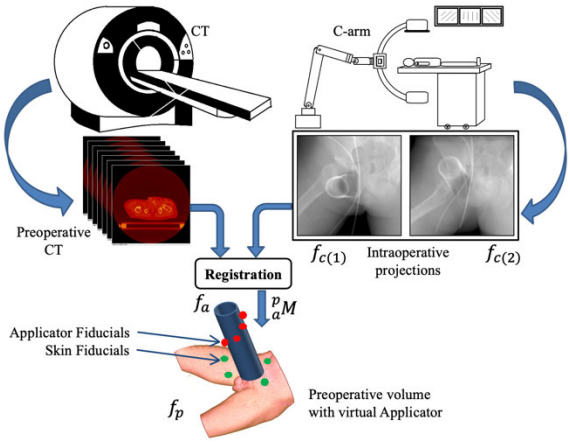

FIGURE 1. Our aim is to place a virtual applicator on preoperative CT to update the IOERT planning through registration of intraoperative projection images and preoperative CT. The proposed protocol includes fiducials on the skin and fiducials on the applicator.

The workflow implies finding rigid transformations between different reference frames denoted f_a for the applicator, f_i for the patient in the intraoperative scenario, f_p for the preoperative CT, $f_{c(1)}, f_{c(2)}, f_{c(3)}, \ldots, f_{c(n)}$ for the n camera frames of the intraoperative projections. The corresponding C-arm radiographs' coordinate reference frames are defined as $f_{r(1)}, f_{r(2)}, \ldots, f_{r(n)}$

Using homogeneous coordinates, the rigid transformation between reference frames can be expressed by 4 × 4 matrices. ${}^{p}_{a}M$ corresponds to the transformation from applicator reference frame (f_a) to the preoperative CT reference frame (f_p). This rigid transformation is the desired solution of the workflow and places the virtual applicator in the preoperative CT for updating the surgical plan.

In a similar way, we define the 4 × 4 matrix ${}^{c(n)}_{a}M$ as the rigid transformation from the applicator frame (f_a) to the camera frame of a certain pose n of the C-arm system $f_{c(n)}$ that expresses the extrinsic camera matrix.

We denote the 3 × 4 matrix ${}^{r(n)}_{c(n)}M$ as the intrinsic matrix that transforms 3D coordinates from the camera frame ($f_{c(n)}$) to the 2D C-arm radiograph image frame ($f_{r(n)}$).

B. C-ARM POSE ESTIMATION

In the first step of our workflow, we use a fiducial-based approach for the pose recovery of the C-arm, ${}^{c(n)}_{a}M$, i.e., the external calibration, for every camera reference. Radiopaque metallic beads, attached to uniquely identify the fiducials in the projections, are used to relate each camera view frame ($f_{c(n)}$) with the applicator reference frame (f_a).

Complex designs involving ellipses, lines [22], [41], and helical lines or two coplanar ellipses [22] have been proposed to guarantee robust segmentation and minimal error when fiducial constellations are used as markers. The following subsections detail the methods to derive each of these transformations from the input information.

In our protocol, we propose to modify a standard cylindrical methacrylate applicator by attaching or embedding metallic spherical beads into the external surface along a helical shape. One bead is of a different size to distinguish it as the first bead in order. The distance between consecutive applicator fiducial markers (AFMs) is varied to avoid possible mistakes identifying fiducials because of geometrical symmetries, while the helix minimizes the risk of occlusions between markers in lateral and top-down views. A CT scan of the applicator allows obtaining the 3D coordinates of the centers of the markers (${}^{a}x_{AFM}$) with respect to the internal frame of reference f_a. In CT, ${}^{a}x_{AFM}$ are estimated with subpixel accuracy as the center of mass of a three-dimensional spherical structure.

First, an intensity threshold I_0 is set to separate the marker region from the main structure of the applicator. Then, a spherical connected component region is calculated followed by an intensity weighting method on each connected region to find each marker centroid $\mathbf{c}_\mathrm{i}$ of the applicator (x_{AFM}) markers.

The following equation determines the center of mass of each marker:

$$\mathrm{c_i} = \frac{\sum_{\mathrm{p}\in\mathrm{R}} (I\,(\mathrm{p}) - I_0)\mathrm{p}}{\sum_{\mathrm{p}\in\mathrm{R}} (I\,(\mathrm{p}) - I_0)}, \tag{1}$$

where $I(\mathrm{p})$ is the intensity of the voxel at position p and R is the connected region where p belongs.

The projection of the AFMs, i.e., their 2D coordinates in the projection images' reference ($\mathrm{f_{r(n)}}$), are denoted as ${}^{r(n)}x_{AFM(j)}, \mathrm{j} \in [1, \mathrm{J}]$, where J is the number of fiducial markers projected on the reference image. In this case, the markers are automatically segmented in the radiographic images using a Hough transform and a support vector machine (SVM) classifier. The Hough transformation detects the circular shapes of the image, and the SVM classifier allows marker projections to be found among the candidates detected by the Hough transformation. The features used by the SVM algorithm were chosen ad hoc and they are: the radius of the circular shape; the minimum, maximum and average values within the shape, and the minimum, maximum and average values in a ring around the shapes detected by the Hough transform.

The C-arm poses ${}^{c(n)}_{a}M$ are estimated individually for each C-arm camera view n using the set of 3D coordinates of the AFMs defined in the applicator frame of reference f_a, ${}^{a}x_{AFM(k)}, k \in [1, K]$ and the set of 2D coordinates of the projections of the fiducial markers in the image frame $f_{r(n)}$, ${}^{r(n)}x_{AFM(j)}, j \in [1, J]$, where J is less than or equal to K. The intrinsic camera calibration ${}^{r(n)}_{c(n)}M$ can be precomputed in advance. Considering that the image distortion of a flat panel C-arm is negligible [42]–[44], in the case of the system used, we did not need to correct it. Therefore, four possible solutions can be obtained for ${}^{c(n)}_{a}M$ in the following equation:

$${}^{r(n)}x_{AFM(j)} = {}^{r(n)}_{c(n)}M \cdot {}^{c(n)}_{a}M \cdot {}^{a}x_{AFM(k)}, \tag{2}$$

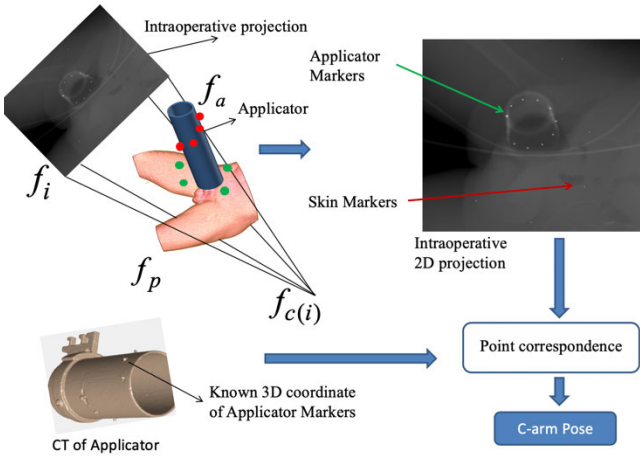

FIGURE 2. From the intraoperative reference images, we first segment and identify fiducials on the applicator (in red). Besides, from the CT of the applicator, the 3D coordinates of the applicator fiducials are already known. A 2D–3D point-correspondence algorithm determines the position and orientation of the C-arm.

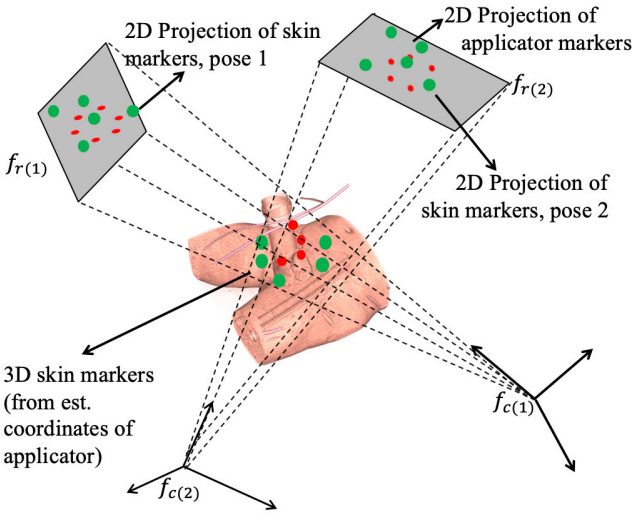

FIGURE 3. 2D–3D point-based registration that uses 3D fiducials on the patient skin ${}^{P}x_{SFM(l)}$ in green, and segmented 2D projections (${}^{r(n)}x_{SFM(q)}$) on C-arm intraoperative images. Two projections are taken from two different poses of the C-arm.

where three 2D–3D correspondences from the set $S = \{(j,k)_1, (j,k)_2 \ldots (j,k)_J\}$ are used that can be disambiguated using a fourth correspondence.

This perspective–three-point (P3P) problem is implemented as a fast-closed-form solution [45] and iteratively computed in the random sample consensus (RANSAC) outlier rejection step [46]. Manual or automatic initial 2D–3D correspondences are not necessary, but all remaining possible pairs are included in the RANSAC algorithm. The only exception is the first AFM that is easily matched because of its difference in size. The remaining possible pairs of set **S** in the P3P problem are randomly chosen for all possible 2D–3D correspondences $(j,k)\, j \in [1, J-1], k \in [1, K-1]$.

Finally, a nonlinear solution of the perspective–n-point problem using all the 2D–3D correspondences, not classified as outliers, reduces the estimated error of the pose recovery [47]. Fig. 3 explains the 2D–3D correspondences.

C. APPLICATOR POSE ESTIMATION

Once the C-arm camera view poses are recovered (${}^{c(n)}_{a}M$), additional fiducial markers are used to position the applicator in the preoperative scenario (the applicator pose) calculating matrix ${}^{p}_{a}M$, i.e., the transformation from f_a to f_p reference frames. In our protocol, we propose to use at least six fiducial markers adhered to the patient's skin via adhesive pads and placed on the skin surrounding the surgical field of interest. These skin fiducial markers (SFMs) consist of metallic beads of different diameters to be distinguished from the AFMs in the radiographic images. Their 3D coordinates in the preoperative CT scan, i.e., in the f_p frame of reference, are denoted as ${}^{p}x_{SFM(l)}, l \in [1, L]$. Their 2D image coordinates in C-arm radiographic images are denoted as ${}^{r(n)}x_{SFM(q)}, q \in [1, Q]$, where Q is less than or equal to L.

To locate the skin markers in the preoperative CT scan, first, thresholding using a 2000 Hounsfield Unit (HU) threshold removes all biological tissues and following a 3D spherical structure estimates the SFMs' centers of mass (Eq. 1). In the radiographic projections, the SFM coordinates, ${}^{r(n)}x_{SFM(q)}$, are detected together with the applicator coordinates, ${}^{r(n)}x_{AFM(j)}$, are detected together with the applicator coordinates, as the center of mass of a spherical structure, but different sizes are used, they are separated using hierarchical agglomerative clustering with unweighted centroids [48].

Because the transformation of the skin markers between the preoperative and intraoperative scenarios may be nonrigid, the method considers more than one projection to estimate first the 3D locations of the skin markers from at least one pair of projections, and then, we estimate the best rigid approximation of this nonrigid transformation by a point-based 3D–3D registration process. As the first step of this process, after recovering the C-arm poses, ${}^{c(n)}_{a}M$, of a projection pair n_A and n_B, we match the SFM projections in both radiographs, ${}^{r(n_A)}x_{SFM}$ and ${}^{r(n_B)}x_{SFM}$ using epipolar geometry [36] by finding the minimal distance between the epipolar lines of ${}^{r(n_A)}x_{SFM}$ in the n_B projection, and vice versa. Once the beads' projections are paired, we can estimate the 3D coordinates of the SFMs in the applicator frame of reference f_a, denoted as ${}^{a}x_{SFM}$, from its projections in two radiographs:

$$\begin{aligned} {}^{r(n_A)}x_{SFM} &= {}^{r(n_A)}_{c(n_A)}M \cdot {}^{c(n_A)}_{a}M \cdot {}^{a}x_{SFM(k)}, \\ {}^{r(n_B)}x_{SFM} &= {}^{r(n_B)}_{c(n_B)}M \cdot {}^{c(n_B)}_{a}M \cdot {}^{a}x_{SFM(k)}. \end{aligned} \tag{3}$$

This triangulation is solved linearly, followed by nonlinear optimization [36], which needs three common SFMs' projections matched on both radiographs to estimate a solution, but using four SFMs is the minimum recommended number for robustness.

Once ${}^{a}x_{SFM(q)}$ are estimated, a point-based 3D–3D registration between ${}^{p}x_{SFM(q)}$ and ${}^{a}x_{SFM(q)}$ is performed. Instead of a classical iterative closest point algorithm, a brute force scheme reports better results and can be calculated in real time because of the small number of SFMs. Therefore, a set of rigid transformations for every permutation of ${}^{p}x_{SFM(q)}$ coordinates are estimated, and the result with the smallest root-mean-square error is chosen that compares the CT coordinates ${}^{p}x_{SFM(q)}$ with respect to the transformed SFMs ${}^{a}x_{SFM(q)}$. The point-based registration result is ${}^{p}_{a}M_{PB}$, which transforms the applicator frame to the preoperative frame, which is our aim for the workflow. Thus, any point ${}^{a}x$ of the applicator can be transformed to a corresponding point ${}^{p}x$ in the preoperative CT as follows:

$$ {}^{p}x = {}^{p}_{a}M_{PB} \cdot {}^{a}x. \tag{4} $$

D. 2D–3D INTENSITY-BASED REGISTRATION

To consider postural changes and surgical procedure that alter the anatomy, a refinement process for ${}^{p}_{a}M_{PB}$ based on 2D–3D intensity-based gray-level registration is necessary to align the internal structures. We assume that a rigid registration referring to the closest rigid structure (bone) provides a good estimation of the applicator position in the preoperative space and that our registration process falls under a rigid transformation that relates 3D coordinates of the CT (f_p) to 2D coordinates in the C-arm radiographs (f_r).

Let us consider the output of the intensity-based 2D–3D registration refinement as M_{θ} . Thus, from Eq. 4:

$$ {}^{p}_{a}M_{GL} = M_{\theta} \cdot {}^{p}_{a}M_{PB}, \tag{5} $$

where ${}^{p}_{a}M_{GL}$ denotes the applicator to intraoperative transformation after gray-level registration.

To perform this process, we have considered the DRR generated from the preoperative CT as the moving images and compared them with the intraoperative C-arm radiograph images that are considered the reference images. Applying masking to confine the processing to the region of interest of both reference 2D images and DRRs increases the probability of getting better registration results and avoids computational overload.

The registration scheme described in the following subsections aims at aligning a 3D preoperative CT to two or more intraoperative C-arm projection images.

1) PREPROCESSING OF THE DATA

As a preprocessing step, the linear attenuation coefficients for the different tissues present in the CT dataset are calculated by converting HU numbers to attenuation values.

The resolution of the CT was chosen to be high enough to ensure DRR projections of comparable resolution to the 2D radiographs; otherwise, local minima because of unmatched and blurred gradients may affect the stability of the registration [49].

Two steps are followed to constrain the registration to the region of interest and to make it more robust in the presence of image content mismatch (a) 2D radiographic masking and (b) 3D CT masking. 2D radiographic masking is performed manually to exclude regions associated with content mismatches such as the regions with instrumentation or surgical implants that typically produce dark shadows because of their metallic property. This manual process is a subjective process. An automatic or semiautomatic segmentation process could be used for this part, but it would increase the computational burden and potential segmentation errors. In contrast, to perform the 3D CT masking, we used an automatic approach by intensity- thresholding to select the bony structures. This intensity- thresholding method is always applicable for our workflow because the background is easily detachable from bone using the threshold 80 HU that is applicable for different patients and studies. To make the procedure robust, it is always better to avoid the effect of nontransparent surgical tables in the preoperative images. In the preoperative CT, a threshold-based segmentation method is used to remove the bed.

2) DRR GENERATION

As a result of the matching procedure of the SFMs, we have an initial transformation that can be considered to generate the DRRs of the 3D dataset to be registered to the 2D C-arm radiographs' reference images. The DRRs are simulated for each C-arm camera view pose to calculate a similarity measure with reference images at the time of optimization. The intensity values for each pixel of the DRR images are computed by summing up the attenuation coefficients associated with each volume element (voxel) along a ray between points of the imaging plane and the imaging source.

Because ${}^{p}_{a}M_{PB}$ (Eq. 4) is known, we can also derive the following,

$$ {}^{r(n)}_{p}M_{PB} = {}^{r(n)}_{c(n)}M \cdot {}^{c(n)}_{a}M \cdot {}^{p}_{a}M_{PB}{}^{-1}, \tag{6} $$

where ${}^{r(n)}_{p}M_{PB}$ denotes the transformation from the preoperative frame to the projection image frame after the second step.

First, n DRRs of the volume are generated from n perspectives using ${}^{r(n)}_{p}M_{PB}$ from Eq. 6. Then, for better matching of the CT-derived DRR images with respect to the C-arm radiography images, the DRRs are normalized to the same intensity ranges.

Even after perfect projection and normalization, there are two main differences between DRR and projection images. One is the presence of surgical instruments in the intraoperative situation when the C-arm projection is taken, which is not present in the preoperative CT-generated DRR. Another difference is the inherent dissimilarity between the simulated CT projections and the C-arm radiographs, as further discussed in the following section.

3) OBJECTIVE FUNCTION

The differences between C-arm projection images and DRRs are because of differences in image formations and changes in the imaged objects. In general, differences in image

formation are caused because of distortions in the projection images, truncation, different resolutions, different X-ray energies between the modalities, heel effect, nonuniformity of the image intensifier response, and postprocessing of the projection images. Furthermore, the proposed DRR simulation does not account for these differences. In contrast, differences because of changes in imaged objects are caused by overlaying and underlying structures, interventional instruments in the field-of-view (FOV), or anatomical deformation [21]. These differences require the use of a heterogeneous monomodal similarity metric.

The combination of similarity metric and optimizer considerably affects the registration performance; the choice of metric depends on the characteristics of the images being registered and their quality. The performance also depends on the actual application. Comparative studies [36], [37] show that metrics based on local intensity correspondence tend to outperform those based on global intensity (e.g., mutual information, MI) in 2D–3D registration [36]. In this work, we proposed using the normalized gradient correlation (NGC) as the similarity metric that enables the comparison of the two types of images despite the mentioned differences.

4) OPTIMIZATION

To ensure convergence, our intensity-based method needs an effective starting point to get an accurate result [32], [35], [50]. Following Otake *et al.* [38], the detector is placed as close as possible to the patient (to maximize radiographic FOV), defining an initial translation along the Z-axis to be equal to half the size of the volume (sometimes termed as patient separation). As described in Subsection B.2, the point-based registration method is used as an initializer, and its main function is to provide an approximate and sufficiently close solution.

The Powell–Brent optimization method is used to obtain the optimal transformation of the CT for alignment. The iterative process calculates the parameters corresponding to the six degrees of freedom of the patient pose. In each iteration, the optimizer modifies the six rigid transformation parameters, and the system generates the new DRRs accordingly. The optimizer repeats the process minimizing the cost function, i.e., finding the maximum similarity between DRRs and the C-arm projections by taking the average of cost function values for all the views until it reaches a convergence criterion. Here, the number of iterations (t) has been used as the stopping criterion for convergence. The number of iterations is decided experimentally by observing typical convergence curves. The optimization problem can be expressed as derivative-based optimization methods including gradient descent and derivative-free optimizations such as the Powell–Brent method, Nelder–Mead simplex method, and the covariance matrix adaptation evolution strategy (CMAES), which are normally used in 2D–3D registration. We used the Powell–Brent method, which is a conjugate direction method and performs a one-dimensional line search for exact minimization.

5) EVALUATION METHODOLOGY

The accuracy of the applicator pose is assessed by acquiring an additional volumetric image, CT or cone-beam CT (CBCT), of the intraoperative scenario for validation purposes only. The positioning error of the actual applicator position retrieved from the volume, with respect to the virtual applicator position calculated following the proposed workflow, was computed. This error was estimated using the Euclidean distance between the coordinates of the point on the applicator's Z-axis, which is closer to the patient and located at the end of the applicator length, and the corresponding point of the calculated virtual applicator position. The orientation errors are assessed by comparing the angle of the estimated applicator longitudinal axis with its actual axis.

Because the intraoperative volume is available, the result of 3D–3D registration between the intraoperative volume and preoperative volume is considered as the ground truth and is stored in two matrices. One is ${}^{i}_{a}M$, where ${}^{i}_{a}M$ is the transformation from the applicator frame of reference f_a to the intraoperative volume reference frame f_i. Another is the 3D–3D registration result ${}^{p}_{i}M$, where ${}^{p}_{i}M$ transforms the intraoperative volume reference frame to the preoperative volume reference frame. Therefore, the final transformation that represents the ground truth can be calculated as follows:

$$ {}^{p}_{a}M_{GT} = {}^{p}_{i}M \cdot {}^{i}_{a}M, \tag{7} $$

where ${}^{p}_{a}M_{GT}$ denotes the applicator to preoperative transformation, defining the ground truth applicator position in the preoperative scenario.

The final error of the proposed workflow can be calculated by measuring the distance of the origin of the applicator axis in the applicator coordinate system, given that our final goal is to position the applicator in the actual position on the preoperative CT image during surgery. Therefore, from Eqs. 6 and 7, we define the following:

$$ \begin{aligned} \text{Error}_{\text{trans}} &= \text{Norm}\left({}^{p}_{a}M_{GL} \cdot {}^{a}x - {}^{p}_{a}M_{GT} \cdot {}^{a}x\right) \\ \text{Error}_{\text{rot}} &= \cos^{-1}\left(\frac{\left({}^{p}_{a}M_{GL} \cdot Z \cdot {}^{p}_{a}M_{GT} \cdot Z\right)}{\left(\| {}^{p}_{a}M_{GL} \cdot Z \| \cdot \| {}^{p}_{a}M_{GT} \cdot Z \|\right)}\right) \end{aligned} \tag{8} $$

where, ${}^{a}x$ is the origin or any point on the applicator axis at which the translational error ($\text{Error}_{\text{trans}}$) is measured in applicator coordinates in homogeneous form. $\text{Error}_{\text{rot}}$ is the rotational error measured at the applicator axis, and Z is the principal axis of the applicator.

6) IMPLEMENTATION

MATLAB was used to design the custom software needed. For the intensity-based registration, Elastix was used. The proposed pipeline has been run on a computer with AMD FX (TM)-8350 Eight-Core Processor, 32 GB of RAM, and Ubuntu 16.04 OS.

IV. EXPERIMENTS AND RESULTS

Different experiments were conducted with a pig lower limb physical phantom dataset to evaluate the proposed algorithm in terms of performance and accuracy. In addition, a proof of

concept experiment using human data of a sarcoma patient was also performed.

Subsection IV-A describes the physical phantom experiment details including data acquisition for preoperative and intraoperative volumes and projection images, workflow setup, registration parameters details, ground truth data, and other details. Subsection IV-B describes the feasibility proof of the concept experiment using human data.

A. EXPERIMENTS WITH THE PHYSICAL PHANTOM

1) DATA ACQUISITION

A complete evaluation of the proposed protocol and methodology was performed through an animal phantom study. For this purpose, an 11-kg pig lower limb was used as a realistic phantom of our patient. The pig lower limb is kept in a plastic tray and fixed with pieces of expanded polystyrene so that it does not move while imaging. A preoperative CT image of the pig lower limb was acquired as the dataset of the preoperative study (Fig. 4a). In addition, a CT of the applicator was acquired to obtain its exact geometry, including the applicator markers located as described in the methodology section (Fig. 4-b). Table 1 summarizes the specifications (dimensions and voxel size) of the preoperative CT and intraoperative CBCT used in the experiments and acquired with conventional clinical scanners.

TABLE 1. Specifications of the dataset used for the experiment.

Volume	Voxel Size (mm)	Dimension (voxels)	Voltage (kVp)	Exposure (mA s)
Preoperative CT	0.98×0.98×1	512×512×480	130	132 ± 62[a]
Intraoperative CT (Ground truth)	1×1×1	410×410×264	70	144 ± 54[a]
Applicator CT	0.25×0.25×1	512×512×248	130	132 ± 62[a]

[a]*Mean ± standard deviation (SD)*

a: PREOPERATIVE CT OF THE PHANTOM

The preoperative CT of the pig lower limb was acquired on a Siemens CT simulator. Skin Markers of size 4 mm were placed on the skin surrounding the area of interest.

b: CT OF IOERT APPLICATOR

A CT of the applicator with 7 cm inner diameter and without any bevel, made of a methacrylate tube was also acquired to extract the exact geometry and location of the AFMs. There were nine Suremark fiducial markers with a diameter size of 2.5 mm and one with a diameter size of 5 mm located (Fig. 4-b) on the surface of the applicator following a spiral layout. The CT of the applicator was acquired on the same Siemens CT simulator after the CT acquisition, the pig lower limb and the applicator were transferred to the LINAC room.

c: INTRAOPERATIVE CBCT DATA

Depending on the IOERT scenario, the applicator was placed on the target region of interest using an articulated arm firmly attached to a fixed structure. In our experiment, the applicator was fixed to the tray that keeps the pig lower limb stationary. To simulate the tumor removal and the surgical procedure, soft tissue of about 3 cm depth was removed from the targeted area (Fig. 4-c). No skin markers were removed in this step, although the relative positions of the markers changed because of soft-tissue movement during tissue removal.

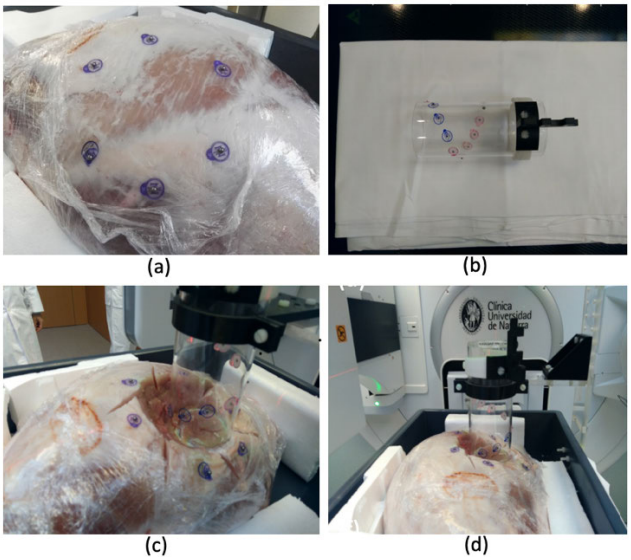

FIGURE 4. (a) Fiducials on skin for preoperative CT acquisition. (b) Applicator with fiducials in spiral disposition. (c) Pig lower limb volume after removal of some tissue to acquire the intraoperative volume with the applicator located on the radiation target area. (d) IOERT setting ready to be acquired with the C-arm radiography system and the CBCT of the intraoperative volume.

The intraoperative CBCT image of the whole IOERT setting (pig with applicator) was obtained with an Elekta Synergy LINAC, which was equipped with an electronic portal imaging device (EPID) and a CBCT system (Fig. 4-d). Both the EPID and the CBCT X-ray unit used a PerkinElmer amorphous silicon detector. The active surface of the detector was 410 mm × 410 mm, and the resolution was 1024 × 1024 pixels. The distance between the source and the imaging panel for the kV and CBCT imaging was 1536 mm.

d: INTRAOPERATIVE C-ARM RADIOGRAPH

Following the proposed protocol and workflow, the intraoperative 2D projection images of the IOERT setting (patient with applicator) were acquired with the same Elekta Synergy LINAC. The 2D C-arm radiographs were acquired at 120 kVp voltage and 5 mA current every 15 degrees (–45, –30, –15, 0, +15, +30, +45) around the radial axis. Fig. 5-a shows some examples of projected radiographs with the skin and the applicator fiducials.

2) WORKFLOW SETUP

The geometric centers of the skin markers, as well as applicator markers, were determined as described in Sections III.B and III.C. In Fig. 5-a, the fiducials and the applicator are visible upon close inspection.

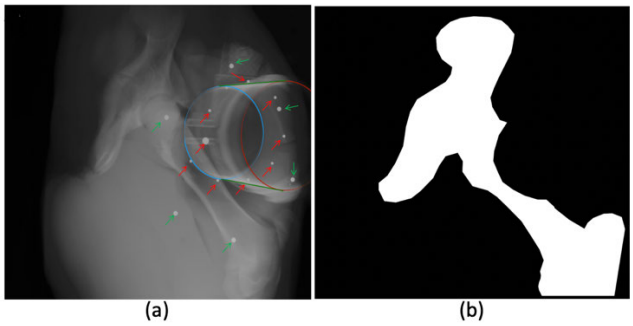

FIGURE 5. **(a) Red arrows pointing at the location of fiducials on the applicator and green arrows pointing at the fiducials on the skin in the intraoperative C-arm radiograph considered the reference images. (b) The binary mask.**

In contrast, as described in the methodology, the fiducials and other instruments were segmented to be masked during the registration process. The segmentation of the region of interest in the radiographs was performed manually, creating a binary mask (Fig. 5-b). As described in the workflow (subsection III.D.1) the mask was applied during the intensity-based registration process so that the objective function calculates nothing outside the area of interest, reducing the local minima and improving the performance of the optimizer.

3) REGISTRATION

For intensity-based registration, the Powell–Brent technique was used as the optimizer, as described in Subsection III.D.4. As a stopping criterion, the number of iterations was fixed to a maximum of 20. The maximum step length was set to 2 mm, the scale factor between translations and rotations was determined automatically, the step tolerance was set to 10^{-4}, and the cost function value tolerance was set to 10^{-6}.

4) DEFINITION OF GROUND TRUTH

CBCT simulator Elekta Synergy was rotated around a fixed isocenter and was confirmed to be regularly geometrically calibrated, providing accurate intrinsic parameter values. Thus, no additional calibration was necessary for our experiment.

Following section III.D.5, to derive the ground truth ${}^{p}_{a}M_{GT}$ (Eq. 7), the matrices ${}^{i}_{a}M$ and ${}^{p}_{i}M$ are computed. First, to find the transformation (${}^{i}_{a}M$), we performed a 3D rigid point-based registration of the applicator markers detected on the intraoperative CBCT, and the applicator markers retrieved from the applicator CT [51].

Second, ${}^{p}_{i}M$ was computed through a 3D–3D registration between the intraoperative CBCT and the preoperative CT. A point-based registration provided the initial transformation using four anatomical points manually identified in the CT and in the intraoperative CBCT. This registration was refined using an intensity-based registration using mutual information and a one-plus-one evolutionary optimizer [52], [53].

The result of this refinement was supervised by visual inspection, achieving a final 3D–3D registration matrix ${}^{p}_{i}M$. By applying Eq. 7, we derived the ground truth transformation ${}^{p}_{a}M_{GT}$ that can be used to calculate the reference pose of the applicator in the preoperative volume.

5) EXPERIMENTS AND RESULTS

a: EXPERIMENT 1: COMBINATION OF SIMILARITY MEASURE AND OPTIMIZER

To ensure that the proper optimizer and similarity metric (subsection III.D.3) was chosen, we performed an experiment to compare the use of NGC with the Powell–Brent optimizer with respect to the use of GD, as proposed by Penney *et al.* [21] and the CMAES optimizer proposed in [41] (Fig. 6 and Fig. 7). NGC, as used by Penney *et al.* [21], refers to the NCC between gradient images that are derived using Sobel operators. The mean gradient value was used to normalize these partial gradients. The cross-correlations are also calculated for the horizontal and vertical gradient images. The sum of these two NCC values defines the NGC.

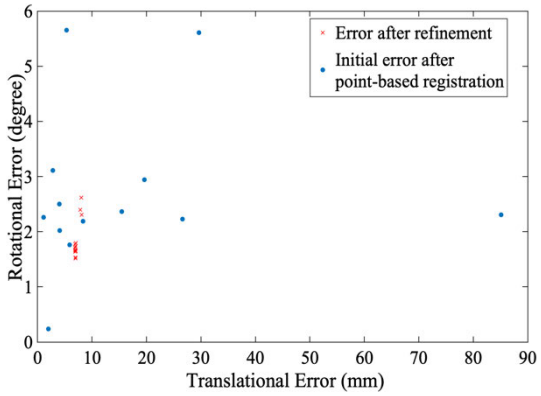

FIGURE 6. **Distribution of initial (red points) and final errors after registration (blue points) when the registration workflow applies GD as the similarity is measured in combination with CMAES as the optimizer.**

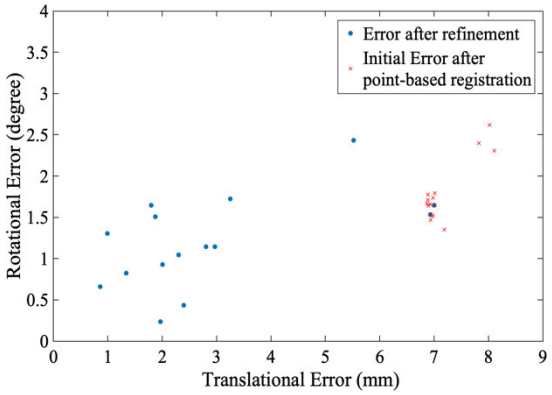

FIGURE 7. **Distribution of initial (red points) and final error after intensity-based registration (blue points) when the registration workflow uses NGC as the similarity measure in combination with Powell–Brent as the optimizer. Note that the axis scales are different from those in Figure 6.**

b: EXPERIMENT 2. EFFECT OF C-ARM RELATIVE POSE OF REFERENCE IMAGES

Seven different poses of the C-arm are considered to acquire seven projections that were used as our reference images. The rotation angle differences among them were 30, 45, 60, 75, and 90 degrees. Random combinations of pairs of projections were used to complete the whole workflow and to analyze whether the resultant applicator pose differed depending on the selected pair of projections or on the angle difference between the projection in each pair. There were 15 such pairs tested, and the results are shown in Fig. 8. The registration failed when the angular separation between projection images were 30, 75, and 90 degrees. In the cases where the angular separation was 45 or 60 degrees, we obtained successful and better registration.

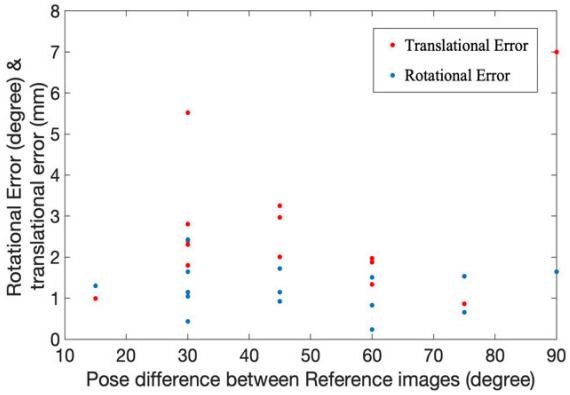

FIGURE 8. Illustration of the distribution of rotational and translational errors after performing the whole workflow. The X-axis defines the angle between reference images and the Y-axis defines the error after registration. Red points are translational error, whereas blue points define angular error.

c: EXPERIMENT 3: WORKFLOW PERFORMANCE

We assessed the global performance through the final error calculation of the whole workflow using the same 15 pairs of images, as shown in Experiment 2. Fig. 9 illustrates the alignment between the preoperative CT images and the intraoperative images to be compared by visual inspection. The registration aligns the bones well in the area of the applicator. Rigid registration does not account for the transformation of other bones outside the region of interest.

To assess performance, the actual applicator position, as retrieved by the ground truth, was compared with the workflow result following the methodology described in subsection III.E. The applicator axis-angle error was measured before and after the registration refinement with respect to the ground truth. The distance error (Eq. 8) was measured at the applicator Z-axis end point closest to the treating area. The intensity-based registration improved the results of the initialization in 12 out of the 15 pairs of images used. The size of the non-masked area covering the projected region of interest in the reference images determined the success of the registration. The error box plots are shown in Fig. 10. There were 10 pairs of images that resulted in a final registration error lower than 3 mm in translation and 2 degrees in rotation.

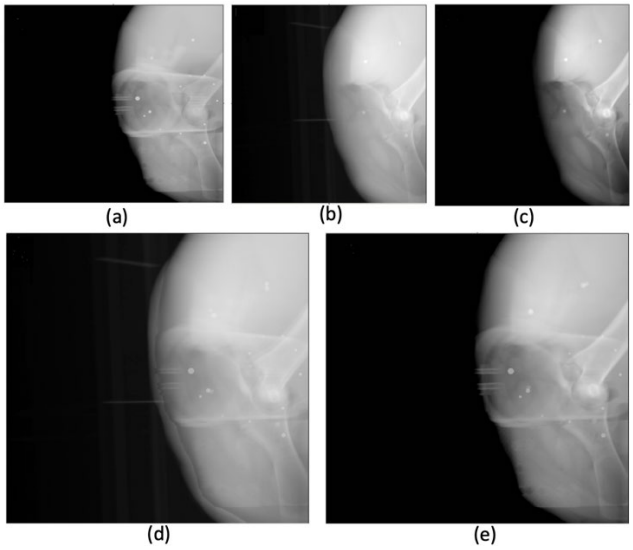

FIGURE 9. (a) Intraoperative projection-reference image. (b) Initial preoperative DRR after initialization. (c) Preoperative DRR after final registration. (d) Comparison between initial DRR and reference image. (e) Comparison between the reference image and DRR after the final registration.

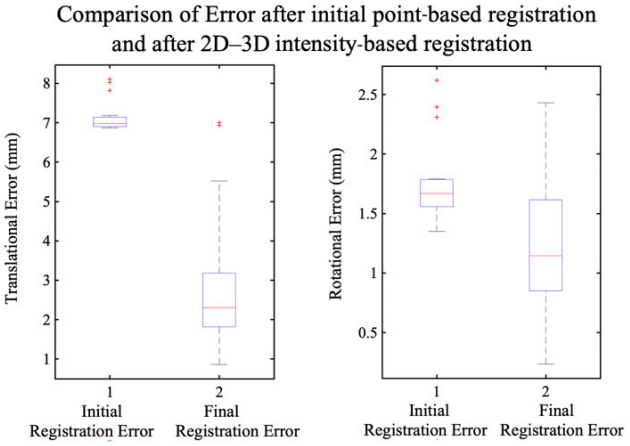

FIGURE 10. Registration accuracy. Translational and rotational error box-and-whisker plots denote the first/third quartiles and min/max values, respectively, with the median marked by a horizontal red line and outliers by crosses.

B. EXPERIMENT WITH HUMAN DATA

In this experiment, we used clinical data from a sarcoma case undergoing IOERT to evaluate the proposed workflow. The study was approved by the Ethics Committee at Hospital General Universitario Gregorio Marañón. Written informed consent was obtained from each patient enrolled for this study.

1) DATA AND SIMULATION

a: PATIENT CT ACQUISITION

CT data were acquired both preoperatively and intraoperatively. A preoperative CT image was acquired using an

Aquilion Large Bore CT simulator (Toshiba, Japan). The IOERT protocol was modified to incorporate the acquisition of an intraoperative CT image of the whole setting (patient and applicator) using the same CT machine and with the specifications listed in Table 2.

TABLE 2. Specification of the human dataset used for the experiment.

Volume	Voxel Size (mm)	Dimension (voxels)	Voltage (kVp)	Exposure (mA s)
Pre	1.21×1.21×2	512×512×435	130	132 ± 62[a]
Intra	0.86×0.86×2	512×512×193	120	144 ± 54[a]

[a]*Mean ± standard deviation (SD)*

Because both the preoperative and intraoperative CT data have a low resolution with a slice thickness of 2 mm, the data were interpolated to a slice thickness of 1 mm.

The original CT datasets did not include skin markers. To replicate the proposed workflow, 2-mm skin markers were added synthetically to both the preoperative and intraoperative CT datasets around the region of interest at six corresponding anatomical points.

b: IOERT APPLICATOR

The IOERT applicator with 7 cm inner diameter and made of methacrylate tube with a 30° bevel angle was placed on the region of interest using an articulated arm that firmly attached the applicator to the CT scanner bed. The maximum distance from the end of the applicator to the tumor bed was 8.5 mm. Because the original acquisition did not include markers on the applicator, nine metallic spherical beads with a diameter of 3 mm and an additional one with a diameter of 4 mm were artificially attached to the external surface of the cylindrical applicator following a helical shape.

c: SIMULATION OF PROJECTION RADIOGRAPHS

The data required for this proof of concept include projection data and a 3D CT dataset of the actual intraoperative scenario, a particular workflow that is not normally available. Therefore, we simulated the C-arm projections of the intraoperative situation as DRRs from the intraoperative CT. Different poses of the C-arm were simulated to obtain several pairs of reference images. The intrinsic parameters for simulating the C-arm images were set as follows: The source-to-detector distance was 1050 mm, source-to-object distance was 800 mm, detector size was 40 cm × 40 cm, or 1024 pixels × 1024 pixels. To generate the DRRs, we used the final ray cast interpolator and the Euler transform. Fig. 11-(a) and Fig. 11-(b) show the fiducials and the applicator on the projected radiograph.

2) EXPERIMENT AND PERFORMANCE

We followed the same workflow set up as described in Subsection IV.A.2. Before registration, the preoperative CT was clipped and masked, selecting mainly the bony structures

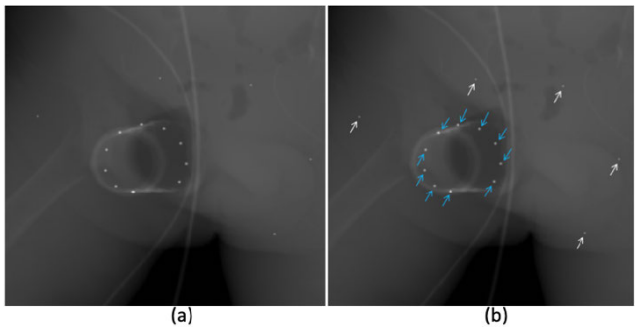

FIGURE 11. (a) Example of a simulated intraoperative radiograph considered as the reference image. (b) Blue arrows point at the location of fiducials in the calibration phantom and white arrows point at the fiducials on the skin. The projection of the applicator is highlighted with an orange line. The fiducials and the applicator are visible upon close inspection.

for DRR generation. The registration parameters used were the same as those described in Subsection IV.A.3.

Random combinations of pairs of projections of human data were used to assess the performance of the workflow. We considered 59 such pairs that had a translational error less than 10 mm and a rotational error less than 2 degrees after point-based registration. The result is shown in Fig. 12.

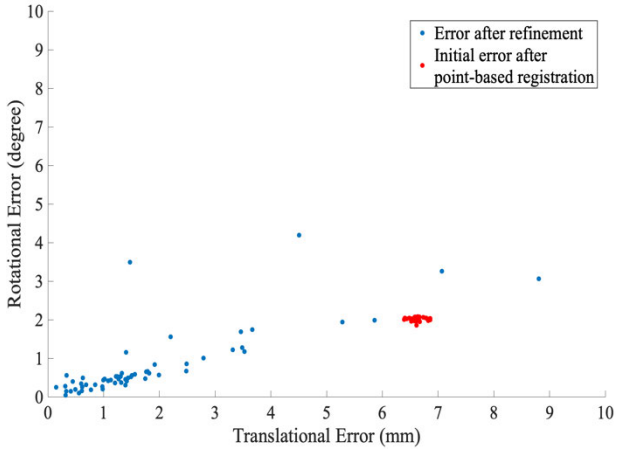

FIGURE 12. Distribution of initial (red points) and final error after registration (blue points) taking several pairs of generated projections from the human data when the registration workflow uses NGC as the similarity measure in combination with Powell–Brent as the optimizer.

Figs. 13 and 14 show the result of the workflow for two different C-arm poses used in the registration process. Fig. 13-d and Fig. 14-d clearly show that a significant initial error exists even after point-based registration (translation error 6.59 mm, angular error 1.97 degrees). The green arrows point to the regions of difference. With the intensity-based registration refinement, the difference is minimized, and the bones overlap perfectly (Fig. 13-e and Fig. 14-e) achieving a final error of 0.55 mm and 0.09 degrees at the applicator base center.

The final position of the applicator in the preoperative volume to update the radiotherapy plan is shown in Fig. 15 is represented in blue and overlaps with the ground truth green

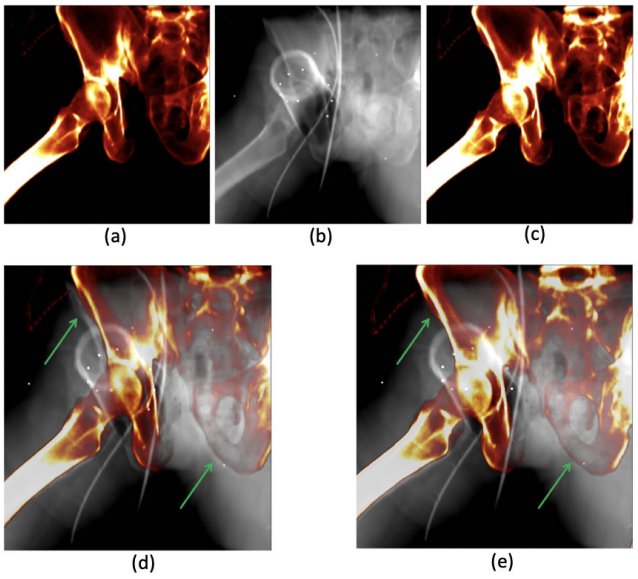

FIGURE 13. Human data experiment. (a) Initial DRR for C-arm pose 1 after point-based registration, (b) reference image 1 with enhanced contrast, (c) final DRR after intensity-based registration, (d) difference between reference 1 and initial DRR, (e) difference between reference 1 and final DRR after registration.

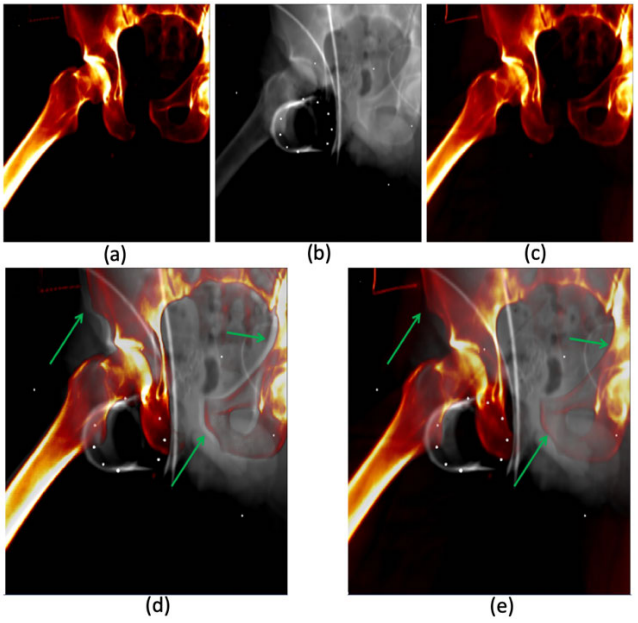

FIGURE 14. Human data experiment. (a) Initial DRR for C-arm pose 2 after point-based registration, (b) reference image 2 with enhanced contrast, (c) final DRR after intensity-based registration, (d) difference between reference 2 and initial DRR, (e) difference between reference 2 and final DRR after registration.

applicator given the small error achieved. The pose difference of the applicator before the refinement intensity-based registration step (red) and the ground truth applicator position (green) is clearly shown in the figure.

V. DISCUSSION

Most recent IOERT protocols include image-based planning performed preoperatively based on a simulation of both the surgical procedure and the radiotherapy set up with the help of preoperative CT images [5], [13]. This preplan considers the patient's anatomy and simulates the surgical cavity, biological fluid accumulation in the surface, bolus, and shielding disks in advance. However, there are always limitations because of the lack of prior knowledge about the final intraoperative situation. Intraoperative imaging before radiation delivery can help to check applicator placement to calculate 3D dose distributions accurately before delivery to ensure safety and proper procedure documentation [3].

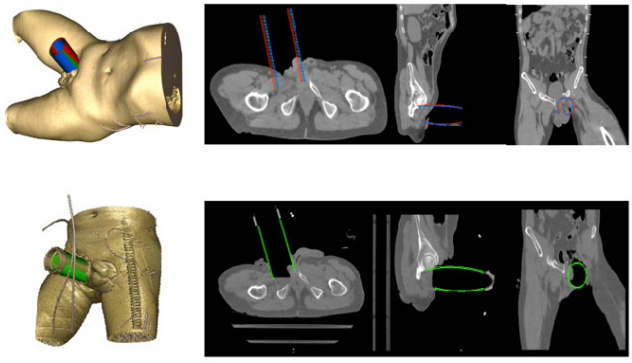

FIGURE 15. Final placement of the applicator in the human data experiment. The green applicator is the ground truth of the applicator position while red and blue correspond to the positions of the applicator before and after the refinement gray level registration step. Upper row represents the preoperative volume, always available to plan and simulate dose distribution to be delivered to the patient. Lower row represents the intraoperative 3D volume acquired during the IOERT procedure, rarely available and used in this work for validation purpose.

In this paper, we have proposed a new protocol and image processing workflow to update the IOERT planning, transporting the actual pose of the applicator to the preoperative CT for dose intraplanning through a hybrid method using a point-based registration followed by an intensity-based 2D–3D registration. A realistic phantom experiment with a pig lower limb has proven the proper performance of the proposed protocol and image processing workflow. The applicator proposed in our workflow has the same geometrical design and structure as the commercial ones but includes attached markers to ensure proper image-based positioning as described in subsection IV.A.1.b. In other contexts, animal experiments have also been presented as reference data for testing different image-guided surgery workflows such as the work and data proposed by Pawiro *et al.* [54] using a cadaver pig head with attached fiducial markers. With this paper, we also make the data available as a new resource. This framework allowed us to prove the performance in the presence of soft-tissue deformations, which is more realistic and challenging.

Moreover, our workflow works without any external tracking system. Our point-based registration step gives an initial registration close to the solution. We have approached this step by implementing a marker-based robust initialization that does not require external tracking systems. In addition, because the distortion in images from flat panel detectors is negligible, we did not need any distortion correction step.

Distortion correction would be required if a non-flat panel C-arm is used. In that case, the distortion parameters are pre-calculated in a previous and independent calibration step, as proposed in [17] using a calibration phantom, and integrated into the proposed workflow as a pre-processing distortion correction step is applied to the C-arm projections. The rest of the workflow remains the same.

Our method can reach the solution while considering any amount of rotation and translation among the different frameworks, which is a great improvement over the existing methods that require tracking to solve this part of the workflow.

3D–3D registration between preoperative CT and intraoperative volume has been considered as the ground truth. An extra CBCT dataset was used for this purpose on the pig lower limb experiment. The CBCT had a low resolution with respect to the preoperative planning CT. The computation of this ground truth transformation could include several sources of inaccuracies involved in the procedure, as follows: intrinsic reconstruction algorithm, limitations of the scanner system and intensity-based registration between two different modalities, as well as the difference in voxel sizes. In any case, the error was assessed to be under 1 mm. For better calculation of the ground truth, the alternative would be to acquire an intraoperative CT.

Our intensity-based registration masking the surgical tools and soft tissues ensured robust registration results. The mask has been created manually, and it can be created automatically starting from the projection of the bone structures in the CT dataset given the initial transformation.

We considered that a final target error of the whole workflow of less than 3 mm of translational error and less than 2 degrees of rotational error was a good performance. In the case of larger applicator sizes, angular errors greater than 2 degrees may affect the radiation dose prescription at the surrounding organs at risk. By considering this target, the performance of the whole workflow and the improvement achieved after the intensity-based registration was confirmed in 12 out of 15 registration experiments (Fig. 10). The reference image pairs that did not show good performance were acquired in such a pose that the projection area of the region of interest was very small. Among the best 12 registrations, 10 minimized the final registration error to a value lower than 3 mm in translation and 2 degrees in rotation. Furthermore, the results comparing the use of NGC and GD as cost functions in our intensity-based 2D–3D registration step demonstrated that NGC is more robust and accurate than GD because it can minimize the error with respect to the initial point-based registration in 12 out of 15 cases (Fig. 7). In contrast, GD was able to minimize the initial error of the point-based registration in only 5 out of 15 cases (Fig. 6), and only 2 of them gave a final registration error within the target considered. By using NGC as the cost function, the average error in translation was 1.97 mm and 0.98 degrees in rotation. In comparison, by using GD (Fig. 10), the average error becomes more than 5 mm in translation and more than 2 degrees in rotation.

The experiment considering different pairs of images did not show a definite relation between the angular separation of reference images with respect to the registration result. A separation of 60 degrees showed better overall results. Our algorithm is independent of the angular separation between projection images, and this does not impose any important requirements. The only important point to consider would be that the FOV of the projection should cover the region of interest as much as possible.

The proof of concept study on human data shows that our algorithm works well in the clinical scenario and that the rigid transformation found in our workflow to update the applicator pose means a good result even in the presence of soft-tissue deformations. As shown in Fig. 12, among 59 registration experiments, 54 minimized both the translational and rotational errors. Among them, 48 experiments resulted in translational errors less than 3 mm and rotational error less than 2 degrees. The average final error in translation is 1.19 mm and in rotation is 0.47 degree. The quality assurance protocol from the Radiotherapy External Beam Quality Assurance Task Group 147 of the American Association of Physicists in Medicine [55] requires a positioning accuracy in the treatment scenario within 2 mm. In both the phantom and human data experiments, the average error was below 2 mm in position of the bevel center and below 2 degrees in orientation, which was measured as the angle between the bevel axis and the longitudinal axis. The errors are small enough compared with the diameter of the applicator (70mm) and within the mentioned acceptable range [55]. The larger error in the pig phantom experiment might be because of a less accurate ground truth calculation. The CBCT image quality and the presence of strike artifacts make it difficult to estimate the center of the metal markers; therefore, the consequent point-based registration accuracy may be affected. In the experiments with human data, both preoperative and intraoperative CTs used to obtain the ground truth have no artifacts and the landmarks can be located with great precision.

This result is far better than our target error. Open challenges may arise when the IOERT implies very large deformations due to the surgical procedure or when a bone structure cannot be identified as a reference. Further research will study how to deal with these nonrigid deformities.

VI. CONCLUSION

In this paper, we propose a novel protocol and workflow to update the IOERT planning with the actual position of the applicator. This workflow achieved accurate and robust registration following two steps, i.e., a point-based registration followed by a 2D–3D intensity-based refinement step. Moreover, our method does not use any external tracking system for calibration. Thus, our method is free from additional problems that usually arise because of the line-of-sight requirement of optical tracking systems or the need for large external fiducials that may occlude the area of interest. Our method shows an improvement over existing methods

because it is more independent of the initial position of the volume. Our method also shows that only two projections can give us optimal registration, thus reducing the exposure of rays on the patient. The combination of NGC as a cost function and Powell–Brent as an optimizer resulted in a robust registration. Future work involves study on solving problems in the presence of large nonrigid deformations and the application of the proposed workflow on an extended human study in the actual clinical setting.

ACKNOWLEDGMENT

The authors would like to thanks Dr. Verónica García Vázquez for her assistance with the collection of patient data at Hospital General Universitario Gregorio Marañón, Spain. They would also like to thank Alvaro Perales Molina of Clinica Universidad de Navarra, Madrid, for his assistance with the collection of animal data.

REFERENCES

[1] M. Lederman, "The early history of radiotherapy: 1895–1939," *Int. J. Radiat. Oncol. Biol. Phys.*, vol. 7, no. 5, pp. 639–648, May 1981.

[2] M. Kusters, V. Valentini, F. A. Calvo, R. Krempien, G. A. Nieuwenhuijzen, H. Martijn, G. B. Doglietto, E. del Valle, F. Roeder, M. W. Buchler, C. J. H. van de Velde, and H. J. T. Rutten, "Results of European pooled analysis of IORT-containing multimodality treatment for locally advanced rectal cancer: Adjuvant chemotherapy prevents local recurrence rather than distant metastases," *Ann. Oncol.*, vol. 21, no. 6, pp. 1279–1284, Jun. 2010.

[3] F. A. Calvo, "Intraoperative irradiation: Precision medicine for quality cancer control promotion," *Radiat. Oncol.*, vol. 12, no. 1, p. 36, Dec. 2017.

[4] F. Schneider, F. Bludau, S. Clausen, J. Fleckenstein, U. Obertacke, and F. Wenz, "Precision IORT–Image guided intraoperative radiation therapy (igIORT) using online treatment planning including tissue heterogeneity correction," *Phys. Medica*, vol. 37, pp. 82–87, May 2017.

[5] F. Calvo, C. Sole, M. González, E. Tangco, J. Lopez-Tarjuelo, I. Koubychine, J. Santos, J. Pascau, R. Herranz, and C. Ferrer, "Research opportunities in intraoperative radiation therapy: The next decade 2013–2023," *Clin. Transl. Oncol.*, vol. 15, no. 9, pp. 683–690, 2013.

[6] C. V. Sole, F. A. Calvo, C. Ferrer, J. Pascau, and H. Marsiglia, "Bibliometrics of intraoperative radiotherapy," *Strahlentherapie und Onkologie*, vol. 190, no. 12, pp. 1111–1116, Nov. 2014.

[7] P. Cherry, and A. M. Duxbury, *Practical Radiotherapy: Physics and Equipment*. Hoboken, NJ, USA: Wiley, 2019.

[8] V. Valentini, M. Balducci, F. Tortoreto, A. G. Morganti, U. De Giorgi, and G. Fiorentini, "Intraoperative radiotherapy: Current thinking," *Eur. J. Surgical Oncol. (EJSO)*, vol. 28, no. 2, pp. 180–185, Mar. 2002.

[9] M. Abe, "Intraoperative radiotherapy—Past, present and future," *Int. J. Radiat. Oncol. Biol. Phys.*, vol. 10, no. 10, pp. 1987–1990, 1984.

[10] R. Soboń, A. Wysocka-Rabin, and N. Golnik, "Design of a positioning system for soft-docking of an intraoperative electron accelerator," *Proc. SPIE*, vol. 8903, Oct. 2013, Art. no. 89031B.

[11] R. W. Janssen, B. A. Faddegon, and W. J. Dries, "Prototyping a large field size IORT applicator for a mobile linear accelerator," *Phys. Med. Biol.*, vol. 53, no. 8, p. 2089, 2008.

[12] S. Nag, C. G. Willett, L. L. Gunderson, L. B. Harrison, F. A. Calvo, and P. Biggs, "IORT with electron-beam, high-dose-rate brachytherapy or low-kV/electronic brachytherapy: Methodological comparisons," in *Intraoperative Irradiation-Tchniques Results*. Humana Press, 2011, pp. 99–115.

[13] J. Pascau, J. A. Santos Miranda, F. A. Calvo, A. Bouché, V. Morillo, C. González-San Segundo, C. Ferrer, J. López Tarjuelo, and M. Desco, "An innovative tool for intraoperative electron beam radiotherapy simulation and planning: Description and initial evaluation by radiation oncologists," *Int. J. Radiat. Oncol. Biol. Phys.*, vol. 83, no. 2, pp. e287–e295, Jun. 2012.

[14] M. F. Valdivieso-Casique, R. Rodríguez, S. Rodríguez-Bescós, D. Lardíes, P. Guerra, M. J. Ledesma, A. Santos, P. Ibáñez, M. Vidal, and J. M. Udías, "RADIANCE-A planning software for intra-operative radiation therapy," *Transl. Cancer Res.*, vol. 4, no. 2, pp. 196–209, 2015.

[15] A. Ciccotelli, S. Carpino, M. D'Andrea, G. Iaccarino, A. Soriani, G. Felici, M. Benassi, and L. Strigari, "EP-1573: Validation of a dedicated intra-operative radiotherapy TPS: An innovative tool for image-guided IORT," *Radiotherapy Oncol.*, vol. 119, pp. S729–S730, Apr. 2016.

[16] T. Jentzsch, K. Sprengel, L. Peterer, L. Mica, and C. M. L. Werner, "3D navigation of endoscopic rhizotomy at the lumbar spine," *J. Clin. Neurosci.*, vol. 23, pp. 101–105, Jan. 2016.

[17] S. Li, Z. Du, and H. Yu, "A robot-assisted spine surgery system based on intraoperative 2D fluoroscopy navigation," *IEEE Access*, vol. 8, pp. 51786–51802, 2020.

[18] J. Weese, G. P. Penney, P. Desmedt, T. M. Buzug, D. L. Hill, and D. J. Hawkes, "Voxel-based 2-D/3-D registration of fluoroscopy images and CT scans for image-guided surgery," *IEEE Trans. Inf. Technol. Biomed.*, vol. 1, no. 4, pp. 284–293, Dec. 1997.

[19] R. M. Comeau, A. F. Sadikot, A. Fenster, and T. M. Peters, "Intraoperative ultrasound for guidance and tissue shift correction in image-guided neurosurgery," *Med. Phys.*, vol. 27, no. 4, pp. 787–800, Apr. 2000.

[20] W. Birkfellner, M. Figl, J. Kettenbach, J. Hummel, P. Homolka, R. Schernthaner, T. Nau, and H. Bergmann, "Rigid 2D/3D slice-to-volume registration and its application on fluoroscopic CT images," *Med. Phys.*, vol. 34, no. 1, pp. 246–255, Dec. 2006.

[21] G. P. Penney, J. Weese, J. A. Little, P. Desmedt, D. L. G. Hill, and D. J. Hawkes, "A comparison of similarity measures for use in 2-D-3-D medical image registration," *IEEE Trans. Med. Imag.*, vol. 17, no. 4, pp. 586–595, Aug. 1998.

[22] A. K. Jain, T. Mustafa, Y. Zhou, C. Burdette, G. S. Chirikjian, and G. Fichtinger, "FTRAC–A robust fluoroscope tracking fiducial," *Med. Phys.*, vol. 32, no. 10, pp. 3185–3198, Sep. 2005.

[23] A. Jain and G. Fichtinger, "C-arm tracking and reconstruction without an external tracker," in *Proc. Int. Conf. Med. Image Comput. Comput.-Assist. Intervent. (MICCAI)*, vol. 4190. Copenhagen, Denmark, 2006, pp. 494–502.

[24] T. S. De Silva, J. Punnoose, A. Uneri, M. Mahesh, J. Goerres, M. W. Jacobson, M. D. Ketcha, A. Manbachi, S. Vogt, and G. Kleinszig, "Virtual fluoroscopy for intraoperative C-arm positioning and radiation dose reduction," *J. Med. Imag.*, vol. 5, no. 1, 2018, Art. no. 015005.

[25] E. Marinetto, D. Garcia-Mato, A. Garcia, S. Martinez, M. Desco, and J. Pascau, "Multicamera optical tracker assessment for computer aided surgery applications," *IEEE Access*, vol. 6, pp. 64359–64370, 2018.

[26] K. M. Langen, T. R. Willoughby, S. L. Meeks, A. Santhanam, A. Cunningham, L. Levine, and P. A. Kupelian, "Observations on real-time prostate gland motion using electromagnetic tracking," *Int. J. Radiat. Oncol. Biol. Phys.*, vol. 71, no. 4, pp. 1084–1090, Jul. 2008.

[27] F. Stevens, M. A. Conditt, N. Kulkarni, S. K. Ismaily, P. C. Noble, and D. R. Lionberger, "Minimizing electromagnetic interference from surgical instruments on electromagnetic surgical navigation," *Clin. Orthopaedics Rel. Res.*, vol. 468, no. 8, pp. 2244–2250, Aug. 2010.

[28] R. Seeberger, G. Kane, J. Hoffmann, and G. Eggers, "Accuracy assessment for navigated maxillo-facial surgery using an electromagnetic tracking device," *J. Cranio-Maxillofacial Surg.*, vol. 40, no. 2, pp. 156–161, Feb. 2012.

[29] G. Zheng, L.-P. Nolte, and S. J. Ferguson, "Scaled, patient-specific 3D vertebral model reconstruction based on 2D lateral fluoroscopy," *Int. J. Comput. Assist. Radiol. Surg.*, vol. 6, no. 3, pp. 351–366, May 2011.

[30] J. Wu, M. Kim, J. Peters, H. Chung, and S. S. Samant, "Evaluation of similarity measures for use in the intensity-based rigid 2D-3D registration for patient positioning in radiotherapy," *Med. Phys.*, vol. 36, no. 12, pp. 5391–5403, Nov. 2009.

[31] D. Tomazevic, B. Likar, T. Slivnik, and F. Pernus, "3-D/2-D registration of CT and MR to X-ray images," *IEEE Trans. Med. Imag.*, vol. 22, no. 11, pp. 1407–1416, Nov. 2003.

[32] H. Livyatan, Z. Yaniv, and L. Joskowicz, "Gradient-based 2-D/3-D rigid registration of fluoroscopic X-ray to CT," *IEEE Trans. Med. Imag.*, vol. 22, no. 11, pp. 1395–1406, Nov. 2003.

[33] G. Zheng, J. Kowal, M. A. González Ballester, M. Caversaccio, and L.-P. Nolte, "(i) registration techniques for computer navigation," *Current Orthopaedics*, vol. 21, no. 3, pp. 170–179, Jun. 2007.

[34] J. Ofverstedt, J. Lindblad, and N. Sladoje, "Fast and robust symmetric image registration based on distances combining intensity and spatial information," *IEEE Trans. Image Process.*, vol. 28, no. 7, pp. 3584–3597, Jul. 2019.

[35] P. Markelj, D. Tomaževič, B. Likar, and F. Pernuš, "A review of 3D/2D registration methods for image-guided interventions," *Med. Image Anal.*, vol. 16, no. 3, pp. 642–661, Apr. 2012.

[36] D. B. Russakoff, T. Rohlfing, A. Ho, D. H. Kim, R. Shahidi, J. R. Adler, and C. R. Maurer, "Evaluation of intensity-based 2D-3D spine image registration using clinical gold-standard data," in *Proc. Int. Workshop Biomed. Image Registration*, Philadelphia, PA, USA, vol. 2717, pp. 151–160, 2003.

[37] W. Birkfellner, M. Stock, M. Figl, C. Gendrin, J. Hummel, S. Dong, J. Kettenbach, D. Georg, and H. Bergmann, "Stochastic rank correlation: A robust merit function for 2D/3D registration of image data obtained at different energies," *Med. Phys.*, vol. 36, no. 8, pp. 3420–3428, Jul. 2009.

[38] Y. Otake, A. S. Wang, A. Uneri, G. Kleinszig, S. Vogt, N. Aygun, L. L. Sheng-fu, J.-P. Wolinsky, Z. L. Gokaslan, and J. H. Siewerdsen, "3D–2D registration in mobile radiographs: Algorithm development and preliminary clinical evaluation," *Phys. Med. Biol.*, vol. 60, no. 5, p. 2075, Feb. 2015.

[39] C. Gendrin, P. Markelj, S. A. Pawiro, J. Spoerk, C. Bloch, C. Weber, M. Figl, H. Bergmann, W. Birkfellner, B. Likar, and F. Pernuš, "Validation for 2D/3D registration II: The comparison of intensity- and gradient-based merit functions using a new gold standard data set," *Med. Phys.*, vol. 38, no. 3, pp. 1491–1502, Feb. 2011.

[40] Y. Otake, A. S. Wang, J. W. Stayman, A. Uneri, G. Kleinszig, S. Vogt, A. J. Khanna, Z. L. Gokaslan, and J. H. Siewerdsen, "Robust 3D–2D image registration: Application to spine interventions and vertebral labeling in the presence of anatomical deformation," *Phys. Med. Biol.*, vol. 58, no. 23, pp. 8535–8553, Nov. 2013.

[41] Y. Otake, M. Armand, R. S. Armiger, M. D. Kutzer, E. Basafa, P. Kazanzides, and R. H. Taylor, "Intraoperative image-based multiview 2D/3D registration for image-guided orthopaedic surgery: Incorporation of fiducial-based C-Arm tracking and GPU-acceleration," *IEEE Trans. Med. Imag.*, vol. 31, no. 4, pp. 948–962, Apr. 2012.

[42] D. A. Jaffray, J. H. Siewerdsen, J. W. Wong, and A. A. Martinez, "Flat-panel cone-beam computed tomography for image-guided radiation therapy," *Int. J. Radiat. Oncol. Biol. Phys.*, vol. 53, no. 5, pp. 1337–1349, Aug. 2002.

[43] J. A. Seibert, "Flat-panel detectors: How much better are they?" *Pediatric Radiol.*, vol. 36, no. 2, p. 173, 2006.

[44] J.-H. Klingler, R. Sircar, C. Scheiwe, E. Kogias, F. Volz, M. T. Krüger, and U. Hubbe, "Comparative study of C-arms for intraoperative 3-dimensional imaging and navigation in minimally invasive spine surgery Part I," *Clin. Spine Surg.*, vol. 30, no. 6, pp. 276–284, Jul. 2017.

[45] L. Kneip, D. Scaramuzza, and R. Siegwart, "A novel parametrization of the perspective-three-point problem for a direct computation of absolute camera position and orientation," in *Proc. CVPR*, Jun. 2011, pp. 2969–2976.

[46] M. A. Fischler and R. C. Bolles, "Random sample consensus: A paradigm for model fitting with applications to image analysis and automated cartography," *Commun. ACM*, vol. 24, no. 6, pp. 381–395, Jun. 1981.

[47] F. Moreno-Noguer, V. Lepetit, and P. Fua, "Accurate Non-Iterative $O(n)$ Solution to the PnP Problem," in *Proc. IEEE 11th Int. Conf. Comput. Vis. (ICCV)*, Rio de Janeiro, Brazil, Oct. 2007, pp. 1–8.

[48] D. Müllner, "Modern hierarchical, agglomerative clustering algorithms," 2011, *arXiv:1109.2378*. [Online]. Available: http://arxiv.org/abs/1109.2378

[49] A. Uneri, Y. Otake, A. Wang, G. Kleinszig, S. Vogt, A. Khanna, and J. Siewerdsen, "3D–2D registration for surgical guidance: Effect of projection view angles on registration accuracy," *Phys. Med. Biol.*, vol. 59, no. 2, p. 271, Dec. 2014.

[50] E. B. van de Kraats, G. P. Penney, D. Tomazevic, T. van Walsum, and W. J. Niessen, "Standardized evaluation methodology for 2-D-3-D registration," *IEEE Trans. Med. Imag.*, vol. 24, no. 9, pp. 1177–1189, Sep. 2005.

[51] K. S. Arun, T. S. Huang, and S. D. Blostein, "Least-squares fitting of two 3-D point sets," *IEEE Trans. Pattern Anal. Mach. Intell.*, vol. PAMI-9, no. 5, pp. 698–700, Sep. 1987.

[52] J. P. W. Pluim, J. B. A. Maintz, and M. A. Viergever, "Mutual-information-based registration of medical images: A survey," *IEEE Trans. Med. Imag.*, vol. 22, no. 8, pp. 986–1004, Aug. 2003.

[53] M. Styner, C. Brechbuhler, G. Szckely, and G. Gerig, "Parametric estimate of intensity inhomogeneities applied to MRI," *IEEE Trans. Med. Imag.*, vol. 19, no. 3, pp. 153–165, Mar. 2000.

[54] S. A. Pawiro, P. Markelj, F. Pernuš, C. Gendrin, M. Figl, C. Weber, F. Kainberger, I. Nöbauer-Huhmann, H. Bergmeister, M. Stock, D. Georg, H. Bergmann, and W. Birkfellner, "Validation for 2D/3D registration I: A new gold standard data set," *Med. Phys.*, vol. 38, no. 3, pp. 1481–1490, Mar. 2011.

[55] T. Willoughby, J. Lehmann, J. A. Bencomo, S. K. Jani, L. Santanam, A. Sethi, T. D. Solberg, W. A. Tomé, and T. J. Waldron, "Quality assurance for nonradiographic radiotherapy localization and positioning systems: Report of task group 147," *Med. Phys.*, vol. 39, no. 4, pp. 1728–1747, Mar. 2012.

SUBHRA S. GOSWAMI received the B.Sc. (Hons.) and M.Sc. degrees in computer science from Visva-Bharati University, in 2003 and 2005, respectively. He is currently pursuing the Ph.D. degree with the Technical University of Madrid, Madrid, Spain. From 2006 to 2007, he was a Data Analyst with the National Institute of Cholera and Enteric Diseases, Indian Council for Medical Research. Since 2007, he has been a Researcher with the Indian Statistical Institute, Kolkata, India, till 2008. From 2008 to 2009, he was a Senior Researcher with the Indian Institute of Management Calcutta, Kolkata. His research interests include image-guided surgery, image-guided intraoperative radiotherapy, and medical imaging.

JUAN E. ORTUÑO received the M.Sc. degree in telecommunication engineering and the Ph.D. degree with quality mention in electronic systems engineering for intelligent environments from the Technical University of Madrid, in 2001 and 2008, respectively. From 2001 to 2008, he was a Research Assistant with the Biomedical Image Technologies Laboratory, Electronic Engineering Department, Technical University of Madrid. Since 2008, he has been a Postgraduate Researcher with the Biomedical Research Networking Center in Bioengineering, Biomaterials and Nanomedicine (CIBER-BBN), Carlos III Health Institute, Madrid, Spain. He has been a Ph.D. Research Fellow with the Department of Biomedical Engineering, School of Medicine, Johns Hopkins University, Baltimore, MD, USA. He has published 20 articles and more than 50 conference proceedings. He is the author of two licensed software packages in medical imaging. His research interests include image processing and multimodal fusion for planning and guidance of minimally invasive cardiac interventions, image segmentation and analysis of dynamic CT angiography, and image reconstruction, simulation, and analysis of positron emission tomography.

ANDRÉS SANTOS (Senior Member, IEEE) received the M.Eng. and Ph.D. degrees from the Universidad Politécnica de Madrid. He is currently a Professor and the Director of the Biomedical Image Technologies Laboratory, Universidad Politécnica de Madrid. He is an International Research Fellow at SRI International, Menlo Park, CA, USA. He has been the Co-Director of a master's program on biomedical technology and instrumentation. He has authored or coauthored over 90 articles in indexed journals on medical imaging and has coordinated more than 50 national and international research projects and technology transfer contracts with private companies. His main research interest includes biomedical image analysis and acquisition.

FELIPE A. CALVO received the degree in medicine and surgery from the Universidad Autónoma de Madrid, in 1978, and the Ph.D. degree from the Universidad de Navarra, Spain, in 1986. He has worked as a Professor with the Department of Radiology and Medical Physics, Universidad de Navarra, from 1987 to 1911; the Department of Radiation Oncology and Nuclear Physics, Hahnemann University, Philadelphia, PA, USA, from 1991 to 1992; and the Department of Radiology and Medical Physics, Faculty of Medicine, Universidad Complutense de Madrid, Spain, from 1993 to 2007. He was the Head of the Department of Oncology, Hospital General Universitario Gregorio Marañón, Madrid, from 1993 to 2017. He is currently the Co-Chairman of the Department of Oncology and the Department of Radiation Oncology and the Clinical Director of the Proton Therapy Unit, Clinica Universidad de Navarra, Madrid. He has authored or coauthored more than 150 articles in indexed journals, more than 50 books, and several proceedings in radiotherapy and medical physics meetings. He is also a Clinical Oncologist interested in therapeutic development in the field of multidisciplinary oncology, in particular, radiotherapy, intraoperative radiotherapy, chemoradiation, and bioassessment of tumor response.

JAVIER PASCAU (Member, IEEE) received the degree in telecommunication engineering from the Universidad Politécnica de Madrid, in 1999, the master's degree in biomedical technology and instrumentation from the Universidad Nacional de Educación a Distancia (UNED), in 2005, and the Ph.D. degree from the Universidad Politécnica de Madrid, in 2006. He is currently an Associate Professor with the Department of Bioengineering and Aerospace Engineering, Universidad Carlos III de Madrid. He is also a Research Fellow with the Instituto de Investigación Sanitaria Gregorio Marañón. He has authored more than 100 papers in indexed journals and conferences and one book. His research interests include multimodal image quantification and registration both in clinical and preclinical applications, surgical guidance by combining image studies and tracking systems, and machine learning methods for medical image analysis.

MARÍA J. LEDESMA-CARBAYO (Member, IEEE) received the M.Eng. degree in telecommunication engineering, in 1998, with a master thesis on medical image analysis, and the Ph.D. degree (Hons.) from the Universidad Politécnica de Madrid, in 2003. She additionally completed two different master programs, Biomedical Engineering and Medical Physics from the University of Patras, Greece, and Bioengineering from UNED, Spain. She is currently an Associate Professor with the Biomedical Image Technologies Laboratory, Universidad Politécnica de Madrid. She has authored or coauthored over 100 publications in indexed journals and conferences. Her main research interest includes biomedical image analysis, especially cardiac and pulmonary imaging, image-guided therapy, microscopy image analysis, registration, and motion estimation and compensation.